Numerical analysis of tiny-focal-spot generation by focusing linearly, circularly, and radially polarized beams through a micro/nanoparticle

Shi, Rui; Wang, Zongzhao; Hung, Shih Te; Hellmann, Christian; Wyrowski, Frank

Important note
To cite this publication, please use the final published version (if applicable).
Please check the document version above.

Numerical analysis of tiny-focal-spot generation by focusing linearly, circularly, and radially polarized beams through a micro/nanoparticle

RUI SHI,[1,2,*] **ZONGZHAO WANG,**[1,2] **SHIH-TE HUNG,**[3] **CHRISTIAN HELLMANN,**[4] **AND FRANK WYROWSKI**[1]

[1]*Applied Computational Optics Group, Friedrich Schiller University Jena, Jena, Germany*
[2]*LightTrans International UG, Jena, Germany*
[3]*Delft Center for System and Control, Delft University of Technology, Delft, The Netherlands*
[4]*Wyrowski Photonics UG, Jena, Germany*
[*]*rui.shi@uni-jena.de*

Abstract: Obtaining a tiny focal spot is desired for super resolution. We do a vectorial numerical analysis of the linearly, circularly, and radially polarized electromagnetic fields being focused through a dielectric micro/nanoparticle of size comparable to the wavelength. We find tiny focal spots (up to $\sim 0.05\ \lambda^2$) can be obtained behind micro/nanoparticles of various shapes, e.g. spherical, disk-shaped, and cuboid micro/nanoparticles. Furthermore, we also investigate the influence of the misalignment of a real lens system on the tiny focal spots. We find that tiny focal spots can still be generated even though they are distorted due to the misalignment.

1.   Introduction

A focal spot with as small a lateral size as possible is desired, not only for high-resolution microscopy [1–3], but also in optical lithography, optical data storage, and laser machining. However, lateral spot size is restricted by the diffraction limit investigated by Rayleigh [4] and Abbe [5]. In recent years, various methods have been proposed to obtain an ever-smaller lateral size of the focal spot. Quabis et.al. found, through numerical investigations, that the focusing of a radially polarized beam with an annular aperture results in an even smaller focal spot ($\sim 0.16\ \lambda^2$) in air compared to the diffraction limit by linear polarization ($\sim 0.26\ \lambda^2$) [6]; later, experimental results measured with the knife-edge method [7,8] by focusing with NA = 0.9, validated the numerical prediction [9]. Additional experiments managed to provide an even smaller focal spot ($\sim 0.07\ \lambda^2$) [10] by focusing in the immersion oil with NA = 1.4. The size of the focal spot when linearly, circularly, and radially polarized fields are used in combination with an annular aperture is investigated numerically in [11] and is reviewed in [12]. Some authors also demonstrated the sub-diffraction focusing by using a mask based on the concept of superoscillation [13–17].

Besides the investigation of the polarization of the beams and the types of apertures/masks which influence the size of the focal spot, other authors added a microsphere in the focal region of the convectional microscopy system, which is called microsphere-based microscopy [18–20], to demonstrate super resolution experimentally. However, the focal spot behind the microsphere was demonstrated numerically only by assuming the ideal plane wave illumination [21,22]. Later an engineered microsphere added in the focal region of a conventional microscopy system with radially polarized beam was proposed [23]. A focal spot, which was called nanojet, with the size $\sim 0.14\ \lambda^2$ behind the engineered microsphere, was demonstrated numerically [23].

In the present work, with a similar aim in mind, we do the vectorial physical-optics modeling of the focusing of an electromagnetic field through a dielectric micro/nanoparticle of size comparable to the wavelength. The focused field on the micro/nanoparticles is obtained with linearly, circularly, and radially polarized input fields with both circular and annular apertures,

shown in Fig. 1. The micro/nanoparticles have spherical, disk, and cuboid shapes. The tiny focal spots with the sizes down to $\sim 0.05\ \lambda^2$ are found in air behind the particles. It is smaller than the previously reported size, $\sim 0.14\ \lambda^2$ with a similar configuration. This merit is addressed for the first time in the literature to the authors' best knowledge. The size of the focal spot behind the micro/nanoparticle is investigated and analyzed. Besides an idealized aplanatic lens which satisfies the Abbe sine condition, shown in Fig. 1, the misalignment of a real lens system, shown in Fig. 2, and its influence on the focal spot behind the micro/nanoparticle are also investigated for the first time to the authors' best knowledge.
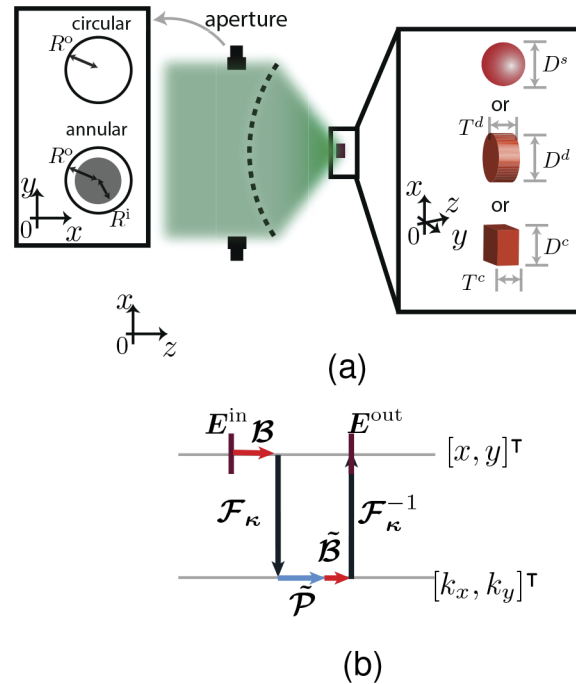
Fig. 1. (a) Schematic of focusing through a micro/nanoparticle by ideal lens. R^{o} is the radius of the aperture. R^{i} is the radius of the inner block. D^s denotes the diameter of the spherical particle. D^d denotes the diameter of the disk-shaped particle. T^d denotes the thickness of the disk-shaped particle. D^c denotes the lateral size of the cuboid particle. T^c denotes the thickness of the cuboid particle. (b) The corresponding field tracing diagram.

This paper is structured as follows: in Sec. 2 the theory we employ for the vectorial physical-optics modeling of the entire system is formulated and presented, complemented by the corresponding field tracing diagram; in Sec. 3 the numerical results of the focusing through different shapes of micro/nanoparticles by an ideal lens are presented and analyzed; in Sec. 4 the numerical results for the influence of the misalignment of a real lens system are presented and analyzed.
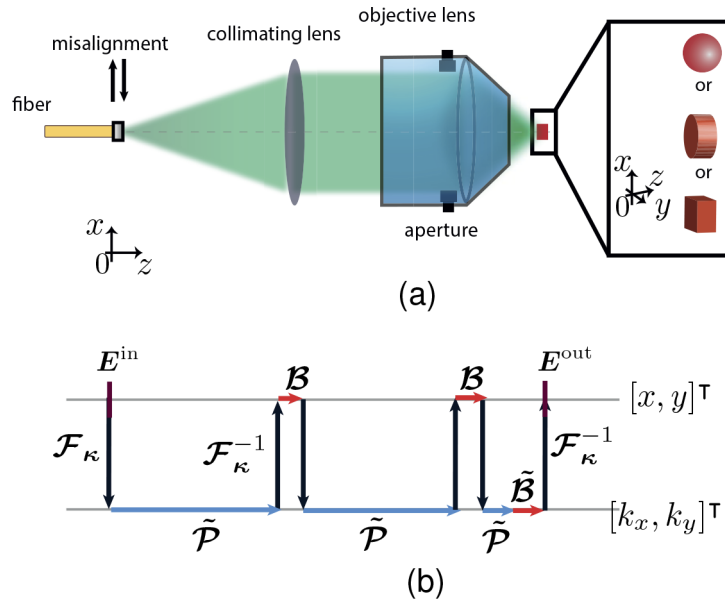
Fig. 2. (a) Schematic of focusing through a micro/nanoparticle by real lens. (b) The corresponding field tracing diagram.

2. Field tracing techniques

To propagate electromagnetic (EM) vectorial fields through an entire optical system rigorously, one can apply different Maxwell's equations solvers [24], e.g. Finite Difference Time Domain (FDTD), Finite Element Method (FEM), Fourier Modal Method (FMM). These methods require heavy computational effort, thus making them impractical for this application. Therefore, we apply the field tracing concept, by tearing the optical system into several regions and, in each region, applying the appropriate field solver for Maxwell's equations. Then the solutions of each of the individual regions are interconnected sequentially or non-sequentially [25]. In this manner the full modeling of the entire system is achieved without sacrificing the calculation accuracy and with full consideration of the vectorial effects in the system, while still having quite reasonable computational speed.

2.1. Source model

To start the field tracing, a vectorial field representing the source light can be generated in the space domain, denoted by $[x, y]^{\mathsf{T}}$, or in the spatial-frequency domain, also called Fourier domain for short, denoted by $[k_x, k_y]^{\mathsf{T}}$ as shown in Fig. 1(b) and Fig. 2(b). x and y are the coordinates of space domain. k_x and k_y are the coordinates of Fourier domain. In this paper, we generate the Gaussian fields as the source in space domain shown by $\boldsymbol{E}^{\text{in}}$ in Fig. 1 and Fig. 2.

For the linearly and circularly polarized sources, the source field is a Hermite Gaussian wave:

$$\boldsymbol{E}_{\perp} = \begin{bmatrix} E_{x0} \exp\left[-\dfrac{x^2 + y^2}{w_0^2}\right] \\ E_{y0} \exp\left[-\dfrac{x^2 + y^2}{w_0^2}\right] \exp\left[i\sigma\right] \end{bmatrix}, \tag{1}$$

where $\boldsymbol{E}_\perp = [E_x, E_y]^\top$ represents the transverse components of the electric field. w_0 is the radius of the waist of the Gaussian wave. σ is the phase delay to define the linear ($\sigma = 0$) and circular ($\sigma = \pi/2$) polarizations.

For the radially polarized source, it is defined as: [3]

$$\boldsymbol{E}_\perp = \begin{bmatrix} E_{x0} \exp\left[-\dfrac{x^2 + y^2}{w_0^2}\right] \mathcal{H}_1\left(\dfrac{\sqrt{2}x}{w_0}\right) \mathcal{H}_0\left(\dfrac{\sqrt{2}y}{w_0}\right) \\[3mm] E_{y0} \exp\left[-\dfrac{x^2 + y^2}{w_0^2}\right] \mathcal{H}_0\left(\dfrac{\sqrt{2}x}{w_0}\right) \mathcal{H}_1\left(\dfrac{\sqrt{2}y}{w_0}\right) \end{bmatrix}, \tag{2}$$

where $\mathcal{H}_0$ and $\mathcal{H}_1$ are the zeroth and first orders of the Hermite polynomial.

2.2. Operators for components

Then the EM field of the source propagates through the entire system. In the framework provided by field tracing, the effects of the curved surface of the lens systems and the micro/nanoparticles are modeled with different operators as indicated in Fig. 1(b) and Fig. 2(b), a mathematical construct which contains the information of how a component of the system modifies an input field. The operators can be calculated by different field solvers, depending on the nature of the components. This concept allows us to combine in a single simulation lens systems and micro/nanoparticles.

We applied this concept to both previously mentioned cases: 1) When the focus of the field on the micro/nanoparticle is obtained by an idealized aplanatic lens, shown in Fig. 1; and (2) when the focus of the field on the micro/nanoparticle is obtained by the misaligned real lens system shown in Fig. 2.

2.2.1. Curved surfaces

In both cases, the focusing systems consist of a high numerical-aperture (NA) objective lens. In the idealized aplanatic case, the objective lens is interpreted as a fictitious curved surface [26]. In the real lens system case, the collimating and objective lenses consist of different complex lenses. The lenses consist of real curved surfaces separating different homogeneous media. In both cases, the operator are computed in the framework of the Local Plane Interface Approximation (LPIA) [26–29] in the space domain, denoted by $\mathcal{B}$ as shown in Fig. 1(b) and Fig. 2(b), to propagate the field through the lenses vectorially with high accuracy and relatively fast computaional speed [29] as:

$$\boldsymbol{E}_\perp^{\text{out}}(\boldsymbol{\rho}^{\text{out}}; z^{\text{out}}) = \mathcal{B}(\boldsymbol{\rho}^{\text{out}}, \boldsymbol{\rho}^{\text{in}}; \Delta Z)\boldsymbol{E}_\perp^{\text{in}}(\boldsymbol{\rho}^{\text{in}}; z^{\text{in}}), \tag{3}$$

where $\boldsymbol{\rho}^{\text{out}} = [x^{\text{out}}, y^{\text{out}}]^\top$ and $\boldsymbol{\rho}^{\text{in}} = [x^{\text{in}}, y^{\text{in}}]^\top$ represent the spatial coordinates at the output and input planes respectively. $\Delta Z = z^{\text{out}} - z^{\text{in}}$ denotes the propagation distance along z direction through the component. z^{in} and z^{out} are the positions of the input and the output electric fields in z directions, respectively.

2.2.2. Micro/nanoparticles

Besides the focusing system with the lenses, in both cases, there are micro/nanoparticles involved near the focal region. The operators for the micro-/nano-structures, denoted by $\tilde{\mathcal{B}}$ as shown in Fig. 1(b) and Fig. 2(b), are calculated rigorously and therefore vectorially in the Fourier domain, to propagate the EM field through the micro/nanoparticles:

$$\tilde{\boldsymbol{E}}_\perp^{\text{out}}(\boldsymbol{\kappa}^{\text{out}}; z^{\text{out}}) = \iint \tilde{\mathcal{B}}(\boldsymbol{\kappa}^{\text{out}}, \boldsymbol{\kappa}^{\text{in}}; \Delta Z)\tilde{\boldsymbol{E}}_\perp^{\text{in}}(\boldsymbol{\kappa}^{\text{in}}; z^{\text{in}})\mathrm{d}\boldsymbol{\kappa}^{\text{in}}, \tag{4}$$

where $\boldsymbol{\kappa}^{\text{out}} = [k_x^{\text{out}}, k_y^{\text{out}}]^\top$ and $\boldsymbol{\kappa}^{\text{in}} = [k_x^{\text{in}}, k_y^{\text{in}}]^\top$ represent the spatial-frequency at the output and input planes respectively. This modeling step is interpreted as several input plane waves with

different spatial frequency interacting with the structure and generating the corresponding output spectrum. The operator for the spherical micro/nanoparticle is calculated by Mie theory [30–32]. And the operators for disk-shaped and cuboid micro/nanoparticles are calculated by FMM with Perfectly Matched Layers (PMLs) based on the S-matrix [24,33–35]. Please note that the operator for a spherical micro/nanoparticle can also be calculated by FMM with PMLs, but with very slow computational speed. Therefore, we take the Mie theory instead.

2.3. Operators for free-space propagation

In-between the different components of the system there are stretches of free space. This also includes the homogeneous media sandwiched between the surfaces of a lens, as well as, evidently, the air filling the gaps between components. We propagate the EM field rigorously via the propagation (P) operator, denoted by $\tilde{\mathcal{P}}$ as shown in Fig. 1(b) and Fig. 2(b), in the Fourier domain:

$$\tilde{\boldsymbol{E}}_{\perp}^{\text{out}}(\boldsymbol{\kappa}^{\text{out}}; z^{\text{out}}) = \tilde{\mathcal{P}}(\boldsymbol{\kappa}^{\text{out}}, \boldsymbol{\kappa}^{\text{in}}; \Delta Z)\tilde{\boldsymbol{E}}_{\perp}^{\text{in}}(\boldsymbol{\kappa}^{\text{in}}; z^{\text{in}}), \tag{5}$$

where $\boldsymbol{\kappa}^{\text{out}} = \boldsymbol{\kappa}^{\text{in}}$. $\tilde{\mathcal{P}}$ is discussed in detail in [36].

2.4. Fourier transforms

After reviewing the field tracing diagram in Fig. 1(b) and Fig. 2(b), we know that the Fourier Transforms (FT) between the space domain $(\boldsymbol{\rho}, \omega)$ and the Fourier domain $(\boldsymbol{\kappa}, \omega)$ are also essential to complete the entire modeling. They are applied to transform the vectorial field between the two domains:

$$\tilde{\boldsymbol{E}}(\boldsymbol{\kappa}) = \mathcal{F}_{\boldsymbol{\kappa}}\left[\boldsymbol{E}(\boldsymbol{\rho})\right], \tag{6a}$$

$$\boldsymbol{E}(\boldsymbol{\rho}) = \mathcal{F}_{\boldsymbol{\kappa}}^{-1}\left[\tilde{\boldsymbol{E}}(\boldsymbol{\kappa})\right]. \tag{6b}$$

In order to accelerate the computational speed of the FT, the Homeomorphic Fourier Transform (HFT) [37,38], also sometimes called geometric Fourier transform [39], on the basis of the stationary phase approximation is performed. The determination of the situation when HFT is performed, is based on a calculation of the accuracy of the HFT with respect to the FFT. The Inverse HFT (IHFT) is applied in stead of Inverse FFT (IFFT) with the same logic.

2.5. Detector model

Focal spot is defined as electric energy density:

$$w_e \propto ||\boldsymbol{E}||^2 = |E_x|^2 + |E_y|^2 + |E_z|^2, \tag{7}$$

where E_z can be obtained by Fourier transform of $\tilde{E}_z$, follwing the equation $E_z = \mathcal{F}_{\boldsymbol{\kappa}}^{-1}\left(\tilde{E}_z\right)$. $\tilde{E}_z$ is calculated by the Gauss's law, $\nabla \cdot \boldsymbol{E} = 0$, of Maxwell's equations in Fourier domain, following the equation:

$$\tilde{E}_z = \frac{k_x\tilde{E}_x + k_y\tilde{E}_y}{-k_z}, \tag{8}$$

where k_z is the z component of the wavevector $\boldsymbol{k}$.

In the following sections, we normalize the above-defined electric energy density to simplify the demonstration of the numerical experimental results as:

$$w_e^{\text{Nor}} = \frac{w_e - w_e^{\text{Min}}}{w_e^{\text{Max}} - w_e^{\text{Min}}}. \tag{9}$$

The size of the spot δ is defined as the area divided by square of the wavelength λ. The area is defined where the energy density is above half the maximum. It is in accordance with the definition in [9–11].

2.6. Summary

How the above-mentioned field tracing techniques are applied to the following numerical experiments is summarized in Table 1. All of the above-mentioned algorithms are implemented in the software VirtualLab Fusion [40], with which all of the following numerical experiments and analyses are performed.

Table 1. Summary of the applications of field tracing techniques.

		$\mathcal{B}$	$\tilde{\mathcal{B}}$	$\mathcal{F}_{\kappa} \& \mathcal{F}_{\kappa}^{-1}$
ideal lens (Fig. 1)	only focusing	LPIA:ideal	no	HFT&IFFT
	through spherical particle	LPIA:ideal	Mie	HFT&IFFT
	through disk-shaped particle	LPIA:ideal	FMM	HFT&IFFT
	through cuboid particle	LPIA:ideal	FMM	HFT&IFFT
real lens (Fig. 2)	only focusing	LPIA:real	no	HFT&IHFT but IFFT for the last one
	through spherical particle	LPIA:real	Mie	HFT&IHFT but IFFT for the last one
	through disk-shaped particle	LPIA:real	FMM	HFT&IHFT but IFFT for the last one
	through cuboid particle	LPIA:real	FMM	HFT&IHFT but IFFT for the last one

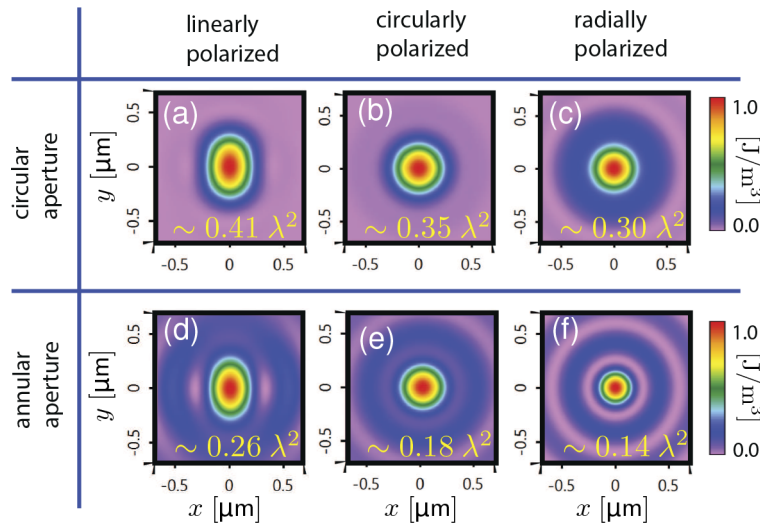## 3. Focusing through a micro/nanoparticle with an ideal lens

In the first simulation, we assume an idealized aplanatic lens, which satisfies the Abbe sine condition. We show the entire simulation results in two steps: 1) only focusing by the lens system to obtain the focused field at the focal plane, and 2) the focused field propagates through the spherical, disk-shaped, and cuboid micro/nanoparticles.

3.1. Focused spots of an ideal lens

We perform the numerical experiments for three different polarizations of the incident field: linearly (in *y* direction), circularly, and radially polarized beams. For each of the polarizations, circular and annular apertures are used. As indicated in Fig. 1(a), the input field is a Gaussian wave with a radius $(1/e^2)$ which is 94% of the radius of the aperture R^{o}. We use the ratio of the radius of the inner block to the radius of the outer aperture, written as $R^{\mathrm{o}}/R^{\mathrm{i}} \times 100\%$ which is illustrated in Fig. 1(a), to define the size of the annular aperture. The size of the annular aperture for linearly, circularly, and radially polarized light are chosen to be 65%, 75%, and 90% respectively. The reason is that the smallest focal spots can be obtained [11] as well as enough energy passes through the annular aperture. The ideal lens has a numerical aperture (NA) of 0.95 in air. The wavelength of the incident field is 632.8 nm in accordance with the parameters in [26,41].

The focal spots produced by the focusing lens system at the focal plane are shown in Fig. 3. By measuring the sizes of the focal spots, we have the same conclusion as in [11] that the size of the radially polarized beam is smaller than the linearly and circularly polarized beams. The reason comes from the smaller size of E_z component which is shown in [11]. The use of an annular aperture further decreases the size of the focal spots by further decreasing the size of E_z

component which is shown in [11]. The sizes of the focal spot are noted in the corresponding figures in yellow.

Fig. 3. Energy densities obtained by only focusing by the idealized aplanatic lens. The sizes of the focal spot are noted in the corresponding figures in yellow.

3.2. Focusing through a micro/nanoparticle

Then we add a spherical, a disk-shaped or a cuboid micro/nanoparticle in the focal region and analyze its effect on the focus. The micro/nanoparticles are dielectric with refractive index $n^p = 1.79$. The size of the spherical particle is characterized by its diameter D^s, shown in Fig. 1(a). The size of the disk-shaped particle is characterized by its diameter D^d and thickness T^d, shown in Fig. 1(a). The size of the cuboid particle is characterized by its lateral lengths D^c which are assumed equal, and thickness T^c, shown in Fig. 1(a). All these size-related quantities are scaled by the wavelength for easy demonstration.
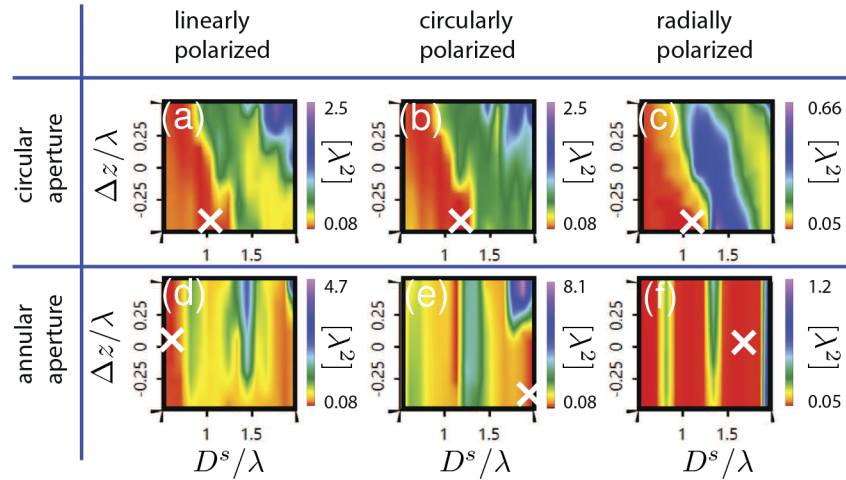
3.2.1. Spherical particle

As shown in Fig. 4, we scan the parameter space defined by the diameter of the spherical particle D^s/λ and the longitudinal distance between the center of the particle and the focal plane $\Delta z/\lambda$. By doing so, we like to find the parameter combination that corresponds to the smallest focal spot behind the spherical particle. Please note that the tiny focal spot is obtained just behind the particle. The position of the tiny focal spot is irrelevant to the focal plane. The focal plane is defined only by the focusing lens, which does not consider the particle yet. As a result of this analysis, we find the smallest spots for linearly and circularly polarized beams in both circular and annular apertures are around $\sim 0.08\ \lambda^2$ in Fig. 4(a), (b), (d), and (e). The smallest spots for radially polarized beams in both circular and annular apertures are around $\sim 0.05\ \lambda^2$ in Fig. 4(c) and (f). They are all beyond the diffraction limit as compared with Fig. 3. The reason is that the resonant effect of the spherical micro/nanoparticle generates evanescent waves which make the focal spots tiny ones. By comparing the circular (Fig. 4(a)-(c)) and annular (Fig. 4(d)-(f)) cases, we find that the size of the focal spot is less sensitive to the longitudinal position of the micro/nanoparticle in the case of an annular aperture. The reason for this is the optical needle effect [42] in the focal region by the lens system when annular aperture is applied.
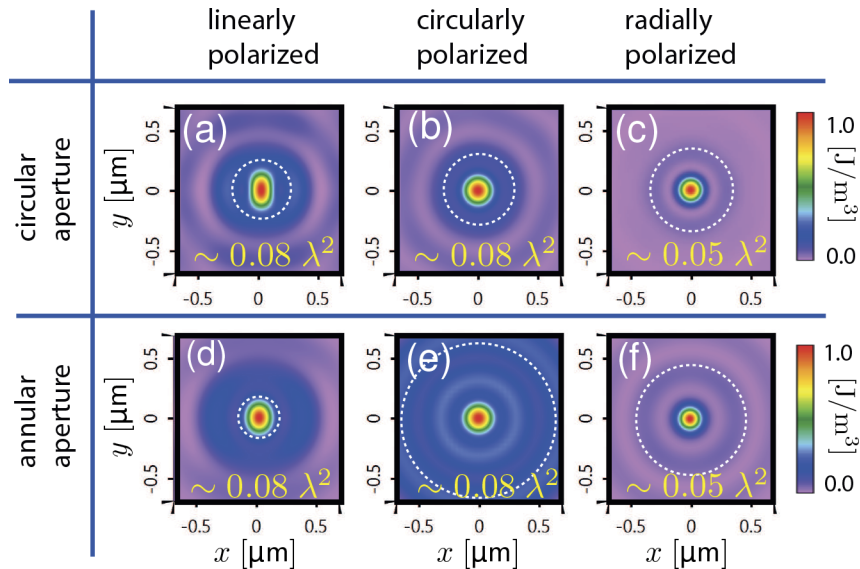
The tiny focal spots are shown in Fig. 5 with the size and longitudinal position marked by "X" in Fig. 4. The dashed white circle represents the projection of the spherical particle on

the detection plane. The size is comparable to the wavelength. The tiny spots in the radially polarized case have less aberration compared to the linearly and circularly polarized cases. By comparing with the diffraction limited focal spots in Fig. 3, the decrease in the size of the focal spot behind the spherical particle is clearly demonstrated.
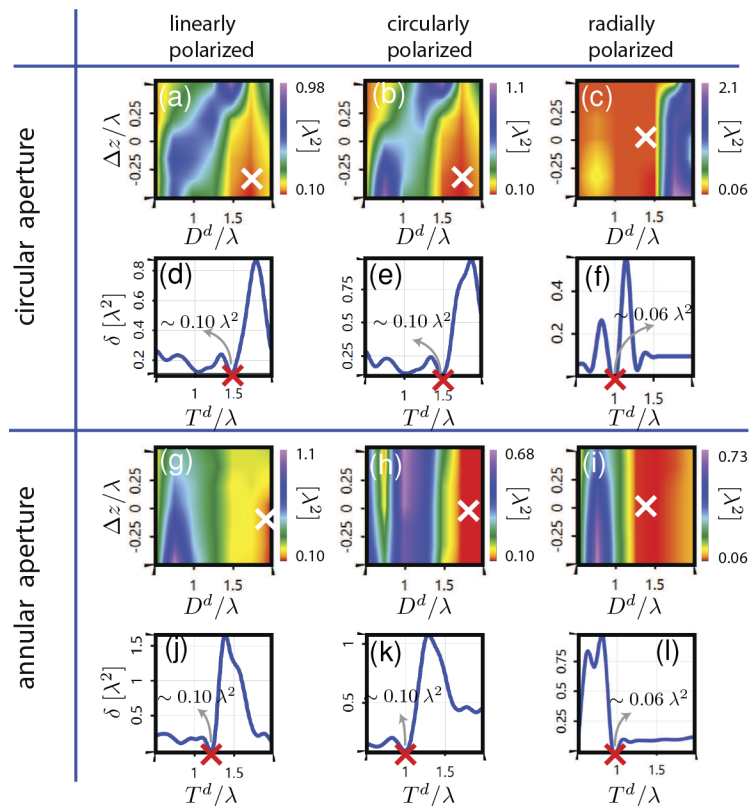

Fig. 4. Scan of the parameter space (diameter of the spherical particle D^s/λ and distance from center of the particle to focal plane $\Delta z/\lambda$) to locate the parameter combination that minimizes the resulting spot size. The "X" is where the parameters are taken for the results in Fig. 5. The color scale represents the spot size.

Fig. 5. Energy densities obtained by focusing the field through spherical micro/nanoparticles. The dashed white circle represents the projection of the spherical particle on the detection plane.
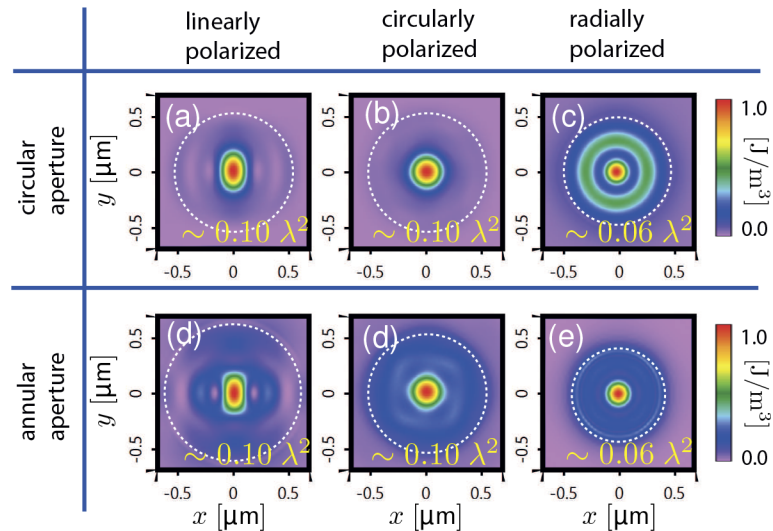
3.2.2. Disk-shaped particle

The spherical particle has concave surfaces. Therefore, it is straightforward to interpret the fact that it has a focusing effect. If the particle is disk-shaped with planar surfaces, does it still have a focusing effect? To answer this question, we follow an analogous procedure to that of the previous subsection 3.2.1. As shown in Fig. 6, first, we scan the diameter D^d of the disk-shaped particle and the longitudinal distance between the center of the particle and the focal plane Δz by making the thickness constant $T^d = 1\ \lambda$. Then, we choose the smallest focal spots as indicated by the white "X" and scan the thickness T^d. The smallest focal spots are selected, as indicated by the red "X". We find the smallest spots for linearly and circularly polarized beams in both circular and annular apertures are around $\sim 0.10\ \lambda^2$ in Fig. 6(d), (e), (j), and (k). The smallest spots for radially polarized beams in both circular and annular apertures are around $\sim 0.06\ \lambda^2$ in Fig. 6(f) and (l). They are larger than in the case of a spherical micro/nanoparticle but still beyond the diffraction limit, which means evanescent waves are also generated in this case. They are generated by resonant effects involving the entire disk, not only its planar surfaces. Without the presence of the side walls, i.e. if instead of the micro/nanoparticle there were only a planar slab, the focusing effect will not occur because no evanescent waves can be generated according to the phase matching condition.


Fig. 6. Scan of the parameter space (diameter of the disk-shaped particle D^d/λ and distance from center of the particle to focal plane $\Delta z/\lambda$ in (a)-(c) and (g)-(i), thickness of the disk-shaped particle T^d/λ in (d)-(f) and (j)-(l)) to locate the parameter combination that minimizes the resulting spot size. The white "X" is where the parameters are taken for the results in the corresponding figures below. The red "X" is where the parameters are taken for the results in Fig. 7.

The tiny focal spots are shown in Fig. 7. The projecion of the disk-shaped particle on the detection plane is indicated by the dashed white circles. On the other hand, the focal spots behind the planar slabs, which have the same material and thickness as the corresponding disk-shaped particles, are shown in Fig. 8 with the size noted in yellow which validates the above deduction numerically.
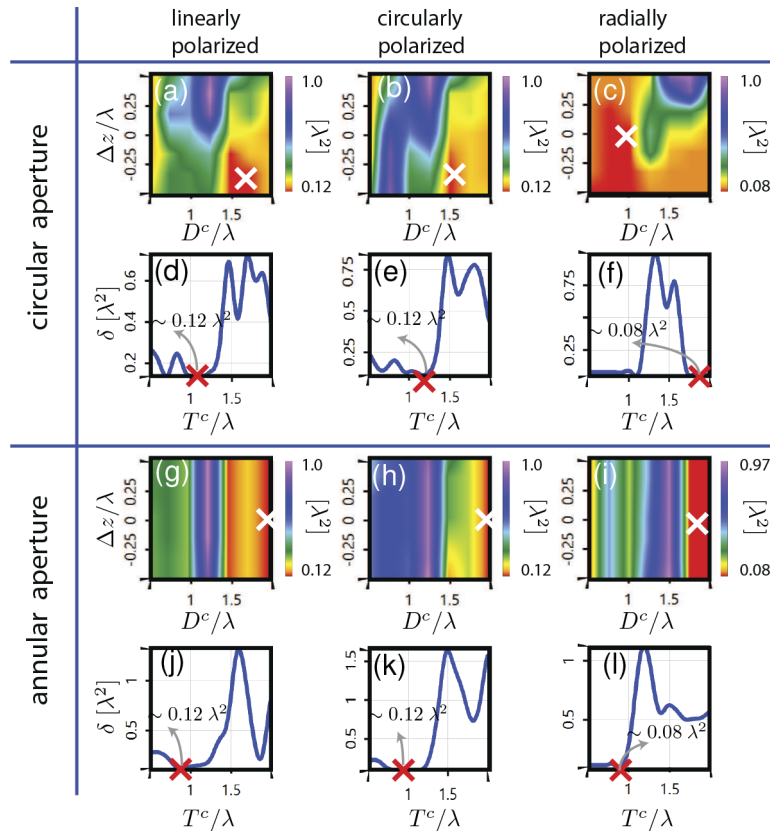

Fig. 7. Energy densities obtained by focusing the field through a disk-shaped micro/nanoparticle. The dashed white circle represents the projection of the disk-shaped particle on the detection plane.
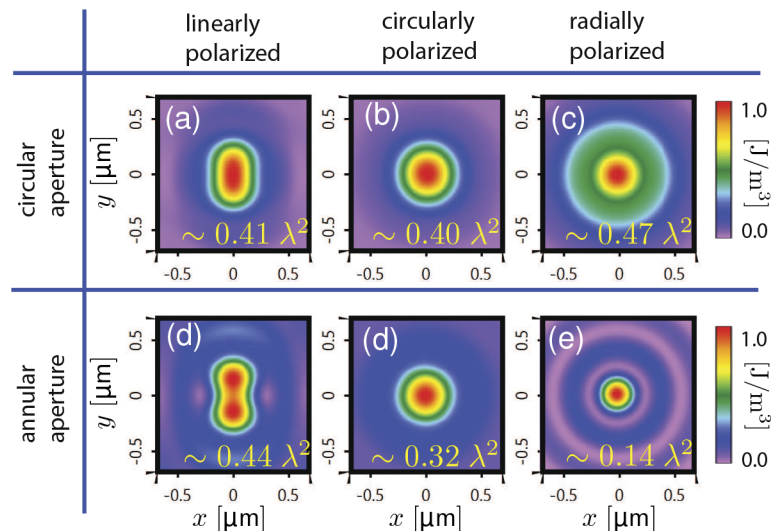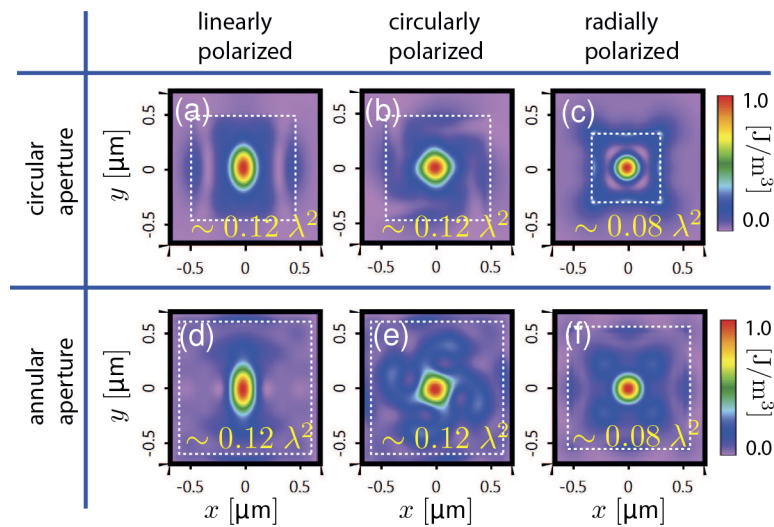

Fig. 8. Energy densities obtained by focusing the field through a planar slab which has the same thickness of the corrensponding disk-shaped micro/nanoparticle in Fig. 7.

3.2.3.   Cuboid particle

The cuboid particle, which is rarely discussed in the literature, should also provide the focusing effect because it has side surfaces which have the potential to provide the resonant effect. Therefore, to prove this hypothesis, we perform the same procedure as before, as shown in Fig. 9. We find the smallest spots for the linearly and circularly polarized beams in both circular and annular apertures are around ∼ 0.12 λ^2 in Fig. 9(d), (e), (j), and (k). The smallest spots for the radially polarized beam in both circular and annular apertures are around ∼ 0.08 λ^2 in Fig. 9(f) and (l). They are larger compared to the spherical and disk-shaped particle cases. The reason might be that the planar surfaces provide a less effective resonant effect than the curved surfaces. And the shape edges and corners introduce more scattering of the light. But the size of the focal spots is still beyond the diffraction limit. The tiny focal spots are shown in Fig. 10.


Fig. 9. Scan of the parameter space (lateral size of the cuboid particle D^c/λ and distance from center of the particle to focal plane $\Delta z/\lambda$ in (a)-(c) and (g)-(i), thickness of the cuboid particle T^c/λ in (d)-(f) and (j)-(l)) to locate the parameter combination that minimizes the resulting spot size. The white "X" is where the parameters are taken for the results in the corresponding figures below. The red "X" is where the parameters are taken for the results in Fig. 10.

Fig. 10. Energy densities obtained by focusing the field through certain cuboid micro/nanoparticles. The dashed white square represents the projection of the cuboid particle on the detection plane.

4. Misalignment investigation by real lenses

When carrying out such an experiment in a real laboratory, naturally a real lens system must be employed. Therefore, we would like to perform a physical-optics simulation of the real lens system to guide the experiment. In this numerical experiment, the collimating lens consists of three spherical surfaces with an effective focal length of 40 mm, as shown in Fig. 11(a). The objective lens, placed 150 mm behind the collimating lens, is apochromatic, consisting of sixteen spherical surfaces with NA = 0.95, as shown in Fig. 11(b). They are taken from the catalog of the commercial company Edmund Optics and from a US patent [43] respectively. The incident fields are Gaussian beams with a waist radius $(1/e^2)$ of $w_0 = 3$ µm generated by a fiber laser. After collimation, the beam has a diameter of $\sim 94\%$ of the entrance pupil diameter of the objective. The wavelength is 632.8 nm. The annular apertures for linearly, circularly, and radially polarized beams are 65%, 75%, and 90% respectively, in accordance with the ideal lens case in Sec. 3.
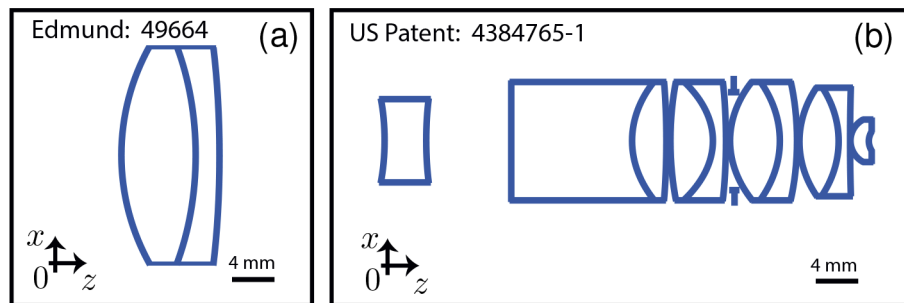

Fig. 11. Cross section of the real lens system including the collimating lens and the objective lens adapted from Ref. [26].

4.1. Focused spots of a real lens

The details of focusing only by the real lens are discussed in [26]. In this paper, we take the case in which the source has a lateral misalignment of −200 μm and 200 μm in *x* and *y* directions respectively. The focused spots are shown in Fig. 12. The focal spots are distorted due to the aberration from the real lens system when the source is misaligned.
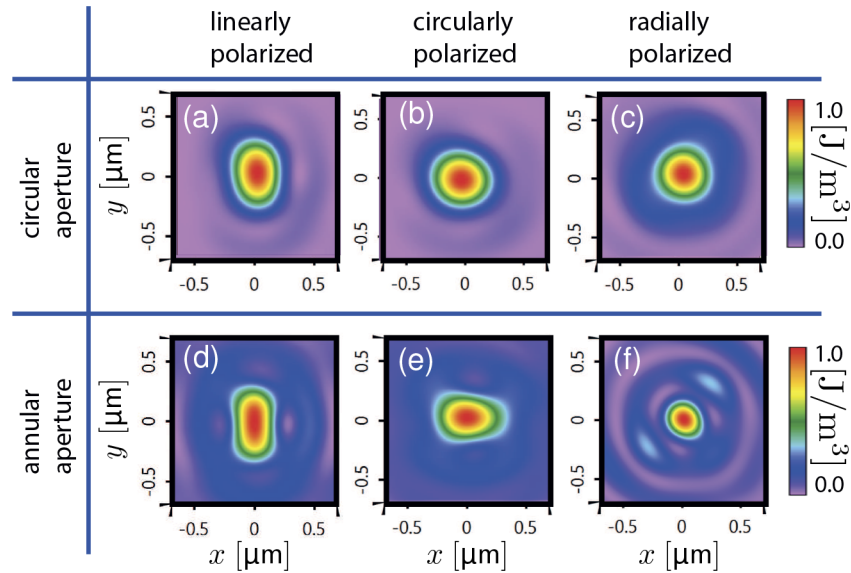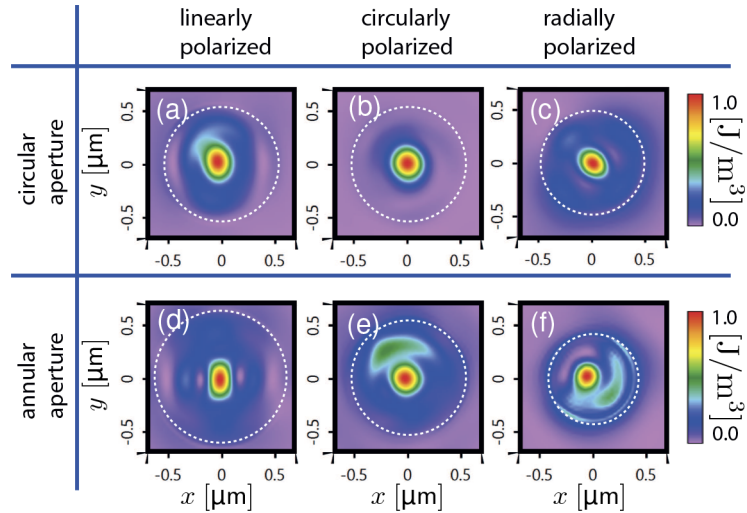

Fig. 12. Distorted energy densities obtained by focusing only with a misaligned real lens.
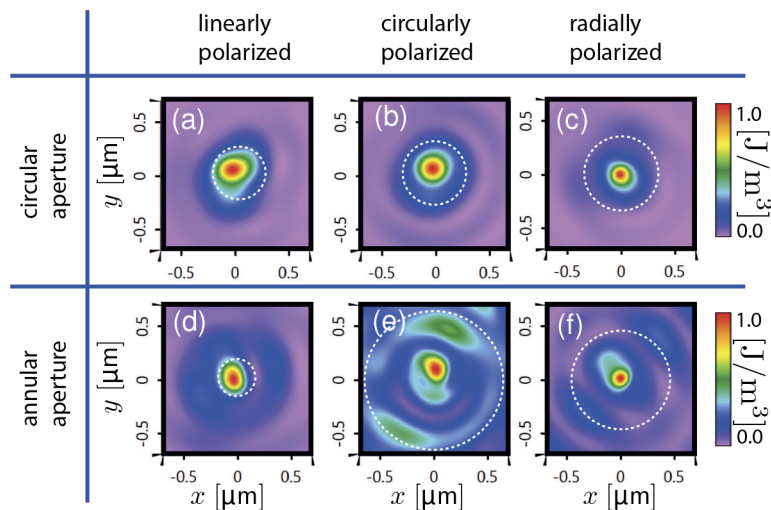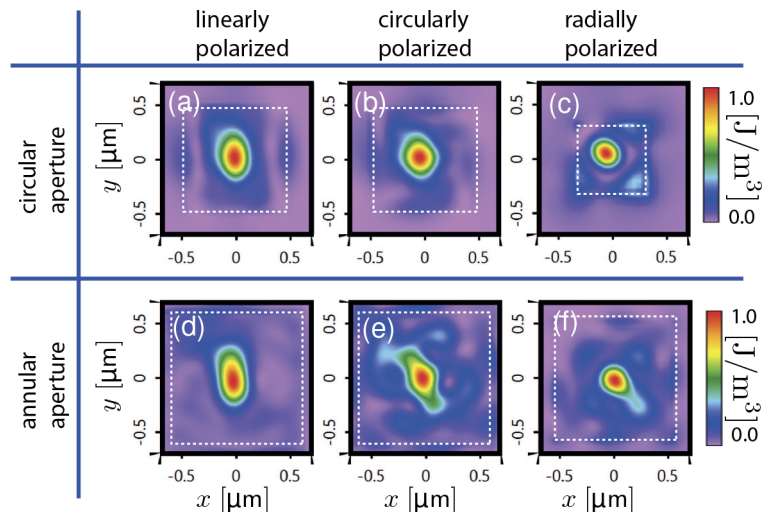

Fig. 13. Distorted energy densities obtained by focusing through the spherical micro/nanoparticles with a misaligned real lens. The dashed white circle represents the projection of the spherical particle on the detection plane.

4.2. *Focusing through a micro/nanoparticle*

Then we focus the distorted focused spots through the previously investigated spherical (Fig. 5), disk-shaped (Fig. 7), and cuboid (Fig. 10) micro/nanoparticles. The center of the micro/nanoparticle coincides with the maximum value of the distorted spots in Fig. 12. The focal spots behind each of the micro/nanoparticles are shown in Fig. 13, Fig. 14, and Fig. 15 for spherical, disk-shaped, and cubic micro/nanoparticles respectively. We can see the tiny focal spots are also distorted as expected. In this real lens situation, we can see from Fig. 13, Fig. 14, and Fig. 15 that the tiny focal spots in the annular aperture case have more distortions compared

Fig. 14. Distorted energy densities obtained by focusing through the disk-shaped micro/nanoparticle with a misaligned real lens. The dashed white circle represents the projection of the disk-shaped particle on the detection plane.

Fig. 15. Distorted energy densities obtained by focusing through the cuboid micro/nanoparticle with a misaligned real lens. The dashed white square represents the projection of the cuboid particle on the detection plane.

with the ones in circular aperture case in general. The reason is that the majority of the electric field in the circular aperture case is in the center part of the lens system. It is relatively more difficult to be influenced by the misalignment of the system. While the majority of the electric field in the annular aperture case is closer to the edge of the lens system, which is easier to be influenced by the misalignment of the system. Even though the distortions appear, the tiny focal spots property is still obtained.

5. Summary and conclusion

We have investigated the focusing of linearly, circularly, and radially polarized beams through spherical, disk-shaped, and cuboid micro/nanoparticles with sizes comparable to the wavelength. The tiny focal spots are generated behind the variously shaped micro/nanoparticles. The size of the tiny focal spots can be reduced down to $\sim 0.05\ \lambda^2$ with a radially polarized beam and a spherical micro/nanoparticle. Linearly and circularly polarized beams combined with disk-shaped and cuboid micro/nanoparticles also generate tiny focal spots which are beyond the diffraction limit due to a resonance effect. The real lens system can distorts the tiny focal spots should there be misalignment in the system. But they are still tiny spots beyond the diffraction limit in the investigated cases.

Disclosures. The authors declare no conflicts of interest.

References

1. B. Richards and E. Wolf, "Electromagnetic diffraction in optical systems. ii. structure of the image field in an aplanatic system," Proc. R. Soc. Lond. A **253**(1274), 358–379 (1959).
2. E. Wolf, "Electromagnetic diffraction in optical systems. i. an integral representation of the image field," Proc. R. Soc. Lond. A **253**(1274), 349–357 (1959).
3. L. Novotny and B. Hecht, Principles of Nano-Optics (Cambridge University Press, 2006).
4. L. Rayleigh, "Xxxi. investigations in optics, with special reference to the spectroscope," The London, Edinburgh, and Dublin Philos. Mag. J. Sci. **8**(49), 261–274 (1879).
5. D. Brocksch, "In memory of ernst abbe," Innovation, The Magazine from Carl Zeiss **15**, 3–23 (2005).
6. S. Quabis, R. Dorn, M. Eberler, O. Glueckl, and G. Leuchs, "Focusing light to a tighter spot," Opt. Commun. **179**(1-6), 1–7 (2000).
7. P. Marchenko, S. Orlov, C. Huber, P. Banzer, S. Quabis, U. Peschel, and G. Leuchs, "Interaction of highly focused vector beams with a metal knife-edge," Opt. Express **19**(8), 7244–7261 (2011).
8. C. Huber, S. Orlov, P. Banzer, and G. Leuchs, "Influence of the substrate material on the knife-edge based profiling of tightly focused light beams," Opt. Express **24**(8), 8214–8227 (2016).
9. R. Dorn, S. Quabis, and G. Leuchs, "Sharper focus for a radially polarized light beam," Phys. Rev. Lett. **91**(23), 233901 (2003).
10. L. Yang, X. Xie, S. Wang, and J. Zhou, "Minimized spot of annular radially polarized focusing beam," Opt. Lett. **38**(8), 1331–1333 (2013).
11. G. M. Lerman and U. Levy, "Effect of radial polarization and apodization on spot size under tight focusing conditions," Opt. Express **16**(7), 4567–4581 (2008).
12. Q. Zhan, "Cylindrical vector beams: from mathematical concepts to applications," Adv. Opt. Photonics **1**(1), 1–57 (2009).
13. H. J. Hyvärinen, S. Rehman, J. Tervo, J. Turunen, and C. J. R. Sheppard, "Limitations of superoscillation filters in microscopy applications," Opt. Lett. **37**(5), 903–905 (2012).
14. M. V. Berry and S. Popescu, "Evolution of quantum superoscillations and optical superresolution without evanescent waves," J. Phys. A: Math. Gen. **39**(22), 6965–6977 (2006).
15. F. M. Huang and N. I. Zheludev, "Super-resolution without evanescent waves," Nano Lett. **9**(3), 1249–1254 (2009).
16. G. Gbur, "Using superoscillations for superresolved imaging and subwavelength focusing," Nanophotonics **8**(2), 205–225 (2018).
17. G. Chen, Z.-Q. Wen, and C.-W. Qiu, "Superoscillation: from physics to optical applications," Light: Sci. Appl. **8**(1), 56 (2019).
18. Z. Wang, W. Guo, L. Li, B. Luk'yanchuk, A. Khan, Z. Liu, Z. Chen, and M. Hong, "Optical virtual imaging at 50 nm lateral resolution with a white-light nanoscope," Nat. Commun. **2**(1), 218 (2011).

19. R. Ye, Y.-H. Ye, H. F. Ma, L. Cao, J. Ma, F. Wyrowski, R. Shi, and J.-Y. Zhang, "Experimental imaging properties of immersion microscale spherical lenses," Sci. Rep. **4**(1), 3769 (2015).
20. H. Zhu, B. Yan, S. Zhou, Z. Wang, and L. Wu, "Synthesis and super-resolution imaging performance of a refractive-index-controllable microsphere superlens," J. Mater. Chem. C **3**(41), 10907–10915 (2015).
21. S. Lee, L. Li, Y. Ben-Aryeh, Z. Wang, and W. Guo, "Overcoming the diffraction limit induced by microsphere optical nanoscopy," J. Opt. **15**(12), 125710 (2013).
22. S. Lee, L. Li, Z. Wang, W. Guo, Y. Yan, and T. Wang, "Immersed transparent microsphere magnifying sub-diffraction-limited objects," Appl. Opt. **52**(30), 7265–7270 (2013).
23. M. Wu, R. Chen, J. Ling, Z. Chen, X. Chen, R. Ji, and M. Hong, "Creation of a longitudinally polarized photonic nanojet via an engineered microsphere," Opt. Lett. **42**(7), 1444–1447 (2017).
24. E. Popov, Gratings: Theory and Numeric Applications (Popov, Institut Fresnel, 2014).
25. M. Kuhn, F. Wyrowski, and C. Hellmann, "Non-sequential optical field tracing," in Advanced Finite Element Methods and Applications, vol. 66 of *Lecture Notes in Applied and Computational Mechanics* T. Apel and O. Steinbach, eds. (Springer, Berlin Heidelberg, 2013), pp. 257–273.
26. R. Shi and F. Wyrowski, "Comparison of aplanatic and real lens focused spots in the framework of the local plane interface approximation," J. Opt. Soc. Am. A **36**(10), 1801–1809 (2019).
27. A. v. Pfeil, F. Wyrowski, A. Drauschke, and H. Aagedal, "Analysis of optical elements with the local plane-interface approximation," Appl. Opt. **39**(19), 3304–3313 (2000).
28. M. R. Foreman and P. Török, "Computational methods in vectorial imaging," J. Mod. Opt. **58**(5-6), 339–364 (2011).
29. R. Shi, C. Hellmann, and F. Wyrowski, "Physical-optics propagation through curved surfaces," J. Opt. Soc. Am. A **36**(7), 1252–1260 (2019).
30. P. Toeroek, P. Higdon, R. Juskaitis, and T. Wilson, "Optimising the image contrast of conventional and confocal optical microscopes imaging finite sized spherical gold scatterers," Opt. Commun. **155**(4-6), 335–341 (1998).
31. H. C. Hulst and H. C. van de Hulst, Light scattering by small particles (Courier Corporation, 1981).
32. J. A. Stratton, Electromagnetic theory, vol. 33 (John Wiley & Sons, 2007).
33. P. Lalanne and E. Silberstein, "Fourier-modal methods applied to waveguide computational problems," Opt. Lett. **25**(15), 1092–1094 (2000).
34. E. Silberstein, P. Lalanne, J.-P. Hugonin, and Q. Cao, "Use of grating theories in integrated optics," J. Opt. Soc. Am. A **18**(11), 2865–2875 (2001).
35. L. Li, "Note on the s-matrix propagation algorithm," J. Opt. Soc. Am. A **20**(4), 655–660 (2003).
36. S. Zhang, D. Asoubar, C. Hellmann, and F. Wyrowski, "Propagation of electromagnetic fields between non-parallel planes: a fully vectorial formulation and an efficient implementation," Appl. Opt. **55**(3), 529–538 (2016).
37. Z. Wang, O. Baladron-Zorita, C. Hellmann, and F. Wyrowski, "Theory and algorithm of the homeomorphic fourier transform for optical simulations," Opt. Express **28**(7), 10552–10571 (2020).
38. O. Baladron-Zorita, Z. Wang, C. Hellmann, and F. Wyrowski, "Isolating the gouy phase shift in a full physical-optics solution to the propagation problem," J. Opt. Soc. Am. A **36**(9), 1551–1558 (2019).
39. F. Wyrowski and C. Hellmann, The geometric fourier transform, Proc. DGaO (2017).
40. Fast physical optics software "Wyrowski VirtualLab Fusion", LightTrans GmbH, Jena, Germany.
41. R. Dorn, S. Quabis, and G. Leuchs, "The focus of light linear polarization breaks the rotational symmetry of the focal spot," J. Mod. Opt. **50**(12), 1917–1926 (2003).
42. H. Wang, L. Shi, B. Lukyanchuk, C. Sheppard, and C. T. Chong, "Creation of a needle of longitudinally polarized light in vacuum using binary optics," Nat. Photonics **2**(8), 501–505 (2008).
43. L. J. Danner, Six-component microscope objective, (1983). US Patent 4,384,765.